

# A Machine Learning Model for the Chemistry of a Solvated Electron

Ruiqi Gao,<sup>1</sup> Pinchen Xie,<sup>2</sup> and Roberto Car<sup>3</sup>

<sup>1</sup>*Department of Electrical and Computer Engineering,  
Princeton University, Princeton, New Jersey 08544, USA*

<sup>2</sup>*Applied Mathematics and Computational Research Division,  
Lawrence Berkeley National Laboratory, Berkeley, California 94720, USA*

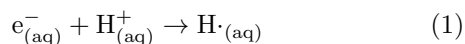
<sup>3</sup>*Department of Chemistry, Princeton University, Princeton, New Jersey 08544, USA*

(Dated: December 1, 2025)

In molecular simulations, machine-learning force fields can achieve ab initio accuracy at a lower cost but remain limited in the explicit modeling of electrons. In this work, we develop an electron-aware machine-learning force field, in which an excess electron of interest is modeled quantum mechanically, while the remaining short-range interactions and long-range Coulombic forces are machine-learned to reproduce a density functional theory calculation. We demonstrate the method on the solvated electron in bulk water and its reaction with a hydronium ion. We identify a proton transfer mechanism by which the excess proton recombines with the electron. We determine the forward reaction rates between 350 K and 450 K from first-passage survival functions, which yield an Arrhenius relationship with an activation energy of 3.2 kcal·mol<sup>-1</sup>, in good agreement with experiment. From an enhanced sampling simulation, we determine the equilibrium constant, and thus the reaction free energy, which is also consistent with experimental measurements.

In recent years, machine-learning (ML) force fields have been developed to learn from non-empirical quantum mechanical methods such as density functional theory (DFT), enabling the simulation of large systems and long timescales with high accuracy [1–4]. These force fields represent the adiabatic potential energy  $E$  as a function of atomic coordinates  $\{\mathbf{R}_i\}$  using neural networks. While successful in many situations, including reactive processes involving bond breaking, these models lack explicit electron-level resolution. Additional ML models have been developed to predict bonding-electron positions in insulators [5], and to incorporate them into long-range Coulomb interactions [6]. However, these do not apply to an electron that is not uniquely associated with an atom. The solvated electron is one notable example. Despite recent attempts with a plain ML force field [7–9] to model its dynamics, a robust electron-aware ML solution has yet to be established [10].

The solvated electron is a localized excess electron in a solution, stabilized by solvent polarization [11, 12]. It is a widely occurring intermediate in radiation-induced chemical and biological processes [12, 13]. In this work, we focus on the solvated electron in water,  $e_{(\text{aq})}^-$ , and its reaction with a hydronium ion:



This produces a hydrogen atom in water. Reaction (1) proceeds on the Born-Oppenheimer ground-state surface and is arguably the simplest reaction of an electron in solution, but its detailed mechanism is still not clear [12]. A historically held view is that  $e_{(\text{aq})}^-$  reacts via electron transfer [14], but more recent DFT-based ab initio molecular dynamics (AIMD) [15] for an excess electron in water clusters [16] suggest a proton-transfer mechanism instead. Quantitative comparisons with the experiments

were not possible because of the high computational cost of simulating such a process in bulk water.

Separately, empirical pseudopotential models have been developed to represent  $e_{(\text{aq})}^-$  [17–19], in which a one-electron Hamiltonian for  $e^-$  is coupled to empirical water models. These methods can reproduce the cavity structure and key spectroscopic properties of  $e_{(\text{aq})}^-$  [12], but lack the first-principles description of all electrons of DFT. Additionally, they are tuned for an isolated  $e_{(\text{aq})}^-$ , so their transferability to reactive environments involving an additional  $\text{H}^+$  is uncertain.

In this work, we address the limitations of both ML force fields and one-electron pseudopotential approaches. We introduce a hybrid method that treats the electron explicitly and uses ML to describe short-range interactions and long-range Coulombic forces. Our simulations support a proton-transfer mechanism for the reaction (1) and yield reaction rates and equilibrium constants in good agreement with experiment. Central to our approach is the following ansatz for the total potential energy:

$$E_{\text{total}} = E_{\text{se}} + E_{\text{lr}} + E_{\text{sr}} \quad (2)$$

Here,  $E_{\text{se}}$  is the ground-state energy of a one-electron Schrödinger equation, which describes the interaction energy between the excess electron and the rest of the system.  $E_{\text{lr}}$  describes the long-range Coulomb interaction within the rest of the system, excluding the excess electron.  $E_{\text{sr}}$  is the short-range energy, represented with a typical neural network potential. In the following, we define these terms in detail and describe the physical motivations that underlie this decomposition.

Firstly, to introduce  $E_{\text{se}}$ , we start with Kohn-Sham DFT. Let  $\psi_e(\mathbf{r})$  be the orbital of the excess electron  $e^-$  and  $n(\mathbf{r})$  be the total electron density of the system.

According to the Kohn-Sham equation,

$$\left(-\frac{1}{2}\nabla^2 + v_{\text{ext}} + v_H[n] + v_{\text{xc}}[n]\right)\psi_{e^-} = \varepsilon\psi_{e^-}, \quad (3)$$

where  $v_{\text{ext}}$  is the external potential produced by the atomic cores (nuclei plus core electrons),  $v_H[n]$  is the Hartree potential of all the electrons and  $v_{\text{xc}}[n]$  is the exchange-correlation potential. Let  $n_{e^-} = |\psi_{e^-}|^2$  be the density of the excess electron. The total density  $n$  can be partitioned into  $n_{e^-} + n_{\text{env}}$ , where  $n_{\text{env}}$  is the density of all the other electrons (the environment). Assuming a weak exchange-correlation interaction between  $e^-$  and the environment, as  $e^-_{(\text{aq})}$  is localized in the cavity of its hydration shell, we approximate  $v_{\text{xc}}[n]\psi_{e^-}$  with  $v_{\text{xc}}[n_{e^-}]\psi_{e^-}$ . Given that  $v_H[n_{e^-}] + v_{\text{xc}}[n_{e^-}] = 0$  for the exact functional, Eq. (3) reduces to

$$\left(-\frac{1}{2}\nabla^2 + v_{\text{ext}} + v_H[n_{\text{env}}]\right)\psi_{e^-} = \varepsilon\psi_{e^-}. \quad (4)$$

$v_{\text{ext}}$  is known for given nuclear positions  $\{\mathbf{R}_i\}$ .  $n_{\text{env}}$  can be approximated using Maximally Localized Wannier Function (MLWF) centers [20]. Specifically, eight valence electrons are associated with each  $\text{H}_2\text{O}$  molecule, and the corresponding MLWF centers can be identified and averaged to what is called a Wannier centroid (WC), as shown in Fig. 1(b). The WC is located near the oxygen atom and carries a charge of  $-8e$ , and its position  $\mathbf{R}^{\text{WC}}$  can be predicted by a neural network [5] based on the atomic neighborhood of each oxygen atom. Together, the total charge density  $\rho_{\text{emb}}$ , which contains all the atomic core and valence electron charges of the system excluding  $e^-$ , can be approximated as

$$\rho_{\text{emb}}(\mathbf{r}) = \sum_i Z_i \rho_s(\mathbf{r} - \mathbf{R}_i) + \sum_j q_j \rho_s(\mathbf{r} - \mathbf{R}_j^{\text{WC}}), \quad (5)$$

with  $Z_i$  being the atomic core charge,  $q_j$  being the WC's charge, and  $\rho_s$  being a spherical Gaussian-smoothed delta function. This approximation is accurate up to the dipole order [6].  $\rho_{\text{emb}}(\mathbf{r})$  generates a Coulomb potential  $V_{\text{emb}}(\mathbf{r}) = -\int d\mathbf{r}' \rho_{\text{emb}}(\mathbf{r}')/|\mathbf{r} - \mathbf{r}'|$ , and Eq. (4) is then approximated by the one-electron Schrödinger equation

$$\left[-\frac{1}{2}\nabla^2 + V_{\text{emb}}\right]\psi_{e^-} = \varepsilon\psi_{e^-}. \quad (6)$$

The ground-state eigenvalue  $\varepsilon$  from Eq. (6) defines  $E_{\text{se}}$ .

We refer to  $V_{\text{emb}}(\mathbf{r})$  as the *embedding potential* for the excess electron. In Fig. 1(a), we show a sample configuration of bulk water containing  $e^-_{(\text{aq})}$  and  $\text{H}_3\text{O}^+$ . The corresponding  $V_{\text{emb}}(\mathbf{r})$  in the cubic periodic cell is shown in Fig. 1(c). Solving Eq. (6) yields our modeled density  $n_{e^-}(\mathbf{r})$  for the excess electron shown in Fig. 1(d). Because of the approximations we have made,  $n_{e^-}(\mathbf{r})$  is not the exact Kohn-Sham density of the excess electron. Nevertheless, in Fig. 1(c), where the frame is centered at the MLWF center of  $e^-_{(\text{aq})}$ , we can see that the modeled  $n_{e^-}(\mathbf{r})$  remains accurately localized around this MLWF

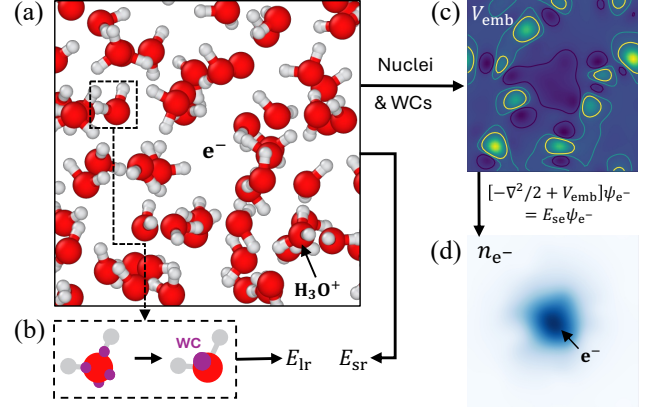


FIG. 1. (a) Sketch of the neighborhood of  $e^-_{(\text{aq})}$ . (b) MLWF centers (small purple dots) and the WC (large purple dot) for one water molecule. (c) The potential  $V_{\text{emb}}$  generated by  $\rho_{\text{emb}}$ ; brighter color means higher energy. (d) Electron density  $n_{e^-}$  obtained from Eq. (6). The heatmaps (c) and (d) display the  $xy$ -plane values centered at the MLWF center of  $e^-$ .

center. This is because  $V_{\text{emb}}$  forms a potential well for the excess electron to localize in the correct position. As long as  $\mathbf{c}_{e^-}$ , the center-of-mass of density  $n_{e^-}$ , is correct, the long-range Coulomb interaction between  $e^-_{(\text{aq})}$  and the rest of the system is correctly captured. Any error due to the approximations is then a short-range effect and will be absorbed into  $E_{\text{sr}}$  with a learnable neural network. This distinguishes our method from all one-electron pseudopotential approaches [17–19], as it is trained to faithfully reproduce the adiabatic potential energy surface of our chosen DFT functional. We note that Eq. (6) can also describe the product state  $\text{H}\cdot_{(\text{aq})}$ , where the potential well in  $V_{\text{emb}}$  and the density  $n_{e^-}$  would localize at the position of the excess proton.

Having established  $E_{\text{se}}$ , we define  $E_{\text{lr}}$  and  $E_{\text{sr}}$  in (2). First,  $E_{\text{lr}}$  is the long-range Coulomb energy of the system excluding  $e^-$ , given by

$$E_{\text{lr}} = \frac{1}{2} \int d\mathbf{r} d\mathbf{r}' \frac{\rho_{\text{emb}}(\mathbf{r})\rho_{\text{emb}}(\mathbf{r}')}{|\mathbf{r} - \mathbf{r}'|}. \quad (7)$$

This is, again, accurate up to dipole-dipole interactions. The sum  $E_{\text{se}} + E_{\text{lr}}$  constitutes the complete long-range electrostatics of the system. Next, the short-range energy satisfies  $E_{\text{sr}} = E_{\text{total}} - E_{\text{se}} - E_{\text{lr}}$ .  $E_{\text{sr}}$  has the typical form  $E_{\text{sr}} = \sum_{i=1}^{N_{\text{atoms}}} E_{\text{NN}}(\{\mathbf{R}_j\}_{j \in \mathcal{N}(i)})$  used in an ML force field, where  $\mathcal{N}(i)$  is the neighborhood of atom  $i$  within a certain radius, and the local energy function  $E_{\text{NN}}$  is represented by a neural network. This is trained to capture all remaining short-range many-body interactions.

In summary, the full model of  $E_{\text{total}}$  is constructed on the basis of two neural networks: one predicts the WCs that underlie  $E_{\text{se}}$  and  $E_{\text{lr}}$ , and another predicts  $E_{\text{sr}}$  directly. In practice, we first train the neural network that describes the WCs using DFT calculations of

the WC positions [5, 20]. With this neural network, we can predict  $\rho_{\text{emb}}$  from a given atomic configuration, and  $E_{\text{se}}$  and  $E_{\text{lr}}$  are obtained from Eq. (6) and (7), respectively. Next, using DFT data for total energy  $E_{\text{total}}$  and atomic forces  $\mathbf{F}_{\text{total}}$ , the neural network representing  $E_{\text{sr}}$  is trained to predict  $E_{\text{total}} - E_{\text{se}} - E_{\text{lr}}$ , as well as short-range forces  $\mathbf{F}_{\text{total}} + \nabla_{\mathbf{R}}E_{\text{se}} + \nabla_{\mathbf{R}}E_{\text{lr}}$ . The derivative  $\nabla_{\mathbf{R}}E_{\text{se}}$  is obtained via the Hellmann–Feynman theorem as  $\langle n_{e^-}, \nabla_{\mathbf{R}}V_{\text{emb}} \rangle$ . The derivative  $\nabla_{\mathbf{R}}V_{\text{emb}}$ , as well as  $\nabla_{\mathbf{R}}E_{\text{lr}}$ , is obtained by directly differentiating the computational workflow, which includes the neural-network prediction of the WCs. Finally, we remark that WCs are determined by the local atomic environment [20], and  $E_{\text{sr}}$  is also expressed as a sum of local contributions. This makes our learned model extensible to larger systems. However, the electron is a global quantity that depends on all atoms in the system to determine where it localizes. We achieve this dependency through  $V_{\text{emb}}$ , a global function of all atoms. This overcomes the locality limitation of standard ML force fields in describing  $e^-$ . In addition, in our model the electrostatic interaction is treated explicitly, providing the physical driving force responsible for the stable localization of  $e^-_{(\text{aq})}$ .

*Numerical implementation.* Our implementation, Deep Potential Long-Range Quantum (DPLR-q), is based on the DP-MP neural network architecture implemented in the deepmd-jax package [9]. We use this architecture for both the WC and short-range models with default hyperparameter settings, including a 6.0 Å neighbor cutoff and one message-passing step. The Schrödinger equation (6) is solved on a real-space grid with an FFT evaluation of the kinetic energy operator. We apply a Rayleigh–Ritz iteration on the span of the current iterate and its kinetic-preconditioned residual to efficiently obtain the ground state. We evaluate  $E_{\text{lr}}$  on the same grid using the Ewald summation. The resulting model maintains the linear-scaling and practical efficiency of standard DP-MP models.

*Model training and validation.* We train our neural networks on the hybrid functional PBEh( $\alpha = 0.4$ ) plus the rVV10 van der Waals correction [21]. This functional has been suggested to reproduce well the energy levels and other properties of  $e^-_{(\text{aq})}$  [22, 23]. Our initial dataset is generated using DFT molecular dynamics simulations of a periodic box containing 64 water molecules, an excess proton, and an excess electron. Details of DFT calculations and model training are given in Appendix A. Several iterations of active learning are performed following the protocol described in Ref. [24]. We test the robustness of our final model over 100 ns of combined simulation time from 350 to 450 K and do not observe any unphysical scenarios. With a 90%–10% train–validation split of the dataset, the WC prediction achieves a root-mean-square error (RMSE) of  $1.0 \times 10^{-3}$  Å in distance, and the short-range energy model has a 0.15 meV/atom

energy RMSE and a 13 meV/Å force RMSE per Cartesian component. We then extend the system to 128 water molecules plus one proton and one electron at the same density and conduct molecular dynamics simulations with our trained model. We observe the same reaction process as in the 64-H<sub>2</sub>O cell. Samples from these 128-H<sub>2</sub>O trajectories form an additional validation set, for which we compute reference DFT data; on this set, our model achieves RMSEs at the same level as those above, confirming the extensibility of our model.

*Reaction mechanism.* Using the molecular dynamics driven by our  $E_{\text{total}}$  model, we accurately learn the reaction process between  $e^-_{(\text{aq})}$  and  $\text{H}^+_{(\text{aq})}$ . Before the reaction,  $\text{H}^+_{(\text{aq})}$  diffuses in water through the Grotthuss hopping mechanism [25]. Meanwhile,  $e^-_{(\text{aq})}$  is localized in a cavity with a radius of  $\sim 2$  Å, surrounded by 4–6 water molecules, and diffuses through the exchange of water molecules in the solvation shell [7, 9, 22].  $\text{H}^+_{(\text{aq})}$  diffuses faster than  $e^-_{(\text{aq})}$ , and we observe a proton-transfer mechanism in the final reaction pathway.

Fig. 2 illustrates the mechanism we observe. (a) The proton diffuses via Grotthuss hopping until it reaches the first coordination shell of  $e^-_{(\text{aq})}$  from the outer side. An H<sub>2</sub>O molecule in the solvation shell of  $e^-_{(\text{aq})}$  has one H pointing towards the electron; with an additional proton, it forms an Eigen-like H<sub>3</sub>O<sup>+</sup> structure. Of the three hydrogens in H<sub>3</sub>O<sup>+</sup>, one points towards the electron, one points to the oxygen from which it comes, and the third points to another water molecule in the surrounding hydrogen-bond network. From here, three pathways can occur. (1) The hydrogen pointing to the electron breaks from H<sub>3</sub>O<sup>+</sup> and forms the product  $\text{H}^+_{(\text{aq})}$ . (2) The hydrogen pointing to the oxygen from which it comes hops back. (3) The hydrogen relays forward to the other neighboring water molecule. We observe all three pathways in our simulations, indicating complex and competing reaction dynamics. Note that the reactants  $e^-_{(\text{aq})}$  and  $\text{H}^+_{(\text{aq})}$  are both strongly hydrated, while the product  $\text{H}^+_{(\text{aq})}$  is hydrophobic. The reaction is driven by solvent polarization and involves substantial solvent reorganization, as is typical of charge-transfer processes in polar solvents [26], and is not a purely diffusion-limited reaction.

*Reaction rate.* Although the reaction is not diffusion-limited and has an energy barrier, the barrier is small enough that the process is accessible within our simulation timescale. We can extract the reaction rate from the first-passage survival probability by simulating an ensemble of independent trajectories. To do this, we prepare an initial ensemble according to the quasi-stationary distribution (QSD) [27], i.e., the distribution of reactant configurations conditioned on not having reacted within a sufficiently long time. This can be efficiently sampled by running a long trajectory with the following modification. Whenever a reaction event is detected during the

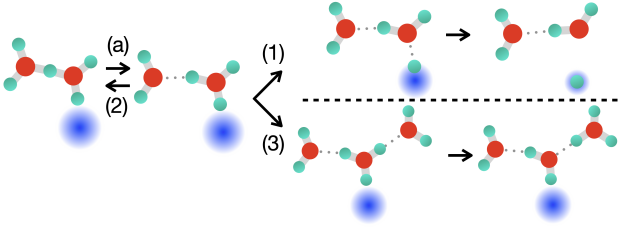


FIG. 2. (a) The proton hops and forms an Eigen-like  $\text{H}_3\text{O}^+$  beside the excess electron. Three outcomes follow: (1) reaction, (2) back-hop, and (3) forward relay. The excess electron (blue) is shown schematically; its spatial extent may exceed the rendering and can be non-isotropic during the reaction [16].

run, we reset to a previous reactant configuration and randomize the velocities. After a relaxation period following each reset, we start recording configurations until the next reaction event. The collection of these surviving trajectory segments will converge to the QSD. Let  $k_2$  be the bimolecular rate constant for the reaction. The reactant concentration is  $V^{-1}$  where  $V$  is the volume of our simulation box. Starting from the QSD, the survival probability  $s$  is an exponential function of time  $\tau$ , given by  $s(\tau) = \exp(-\lambda\tau)$  with  $\lambda = k_2V^{-1}$ . We run  $N_{\text{traj}}$  independent trajectories starting from the QSD up to a right-censoring time  $\tau_{\text{max}}$  when at least half of the trajectories have reacted. We record the time-to-reaction  $\tau_i$  and set  $\tau_i = \tau_{\text{max}}$  for a trajectory without a reaction. Using the maximum-likelihood estimator  $\hat{\lambda} = (1 - \hat{s}(\tau_{\text{max}}))/\langle\tau_i\rangle$ , where  $1 - \hat{s}(\tau_{\text{max}})$  is the fraction of trajectories that have reacted by  $\tau_{\text{max}}$ , we obtain  $\lambda$  and thus  $k_2$ .

We perform this procedure at temperatures of 350, 400, and 450 K [28] using a system of 64, 128, 256, and 512  $\text{H}_2\text{O}$  molecules with one proton and one electron. For each condition, we sample from its QSD and run  $N_{\text{traj}} = 2000$  independent trajectories. The obtained  $k_2$  values are extrapolated to the dilute limit by a linear fit against the inverse box length, and our result is shown in Fig. 3(a). An Arrhenius behavior ( $k_2 \propto e^{-E_a/RT}$ ) is observed, with the activation energy  $E_a = 3.2 \text{ kcal}\cdot\text{mol}^{-1}$  (0.14 eV). This is in good agreement with experimental measurements [29, 30], where the results in Ref. [29] at 400 K correspond to  $E_a = 3.4 \text{ kcal}\cdot\text{mol}^{-1}$ , and Ref. [30] reports  $E_a = 2.4 \text{ kcal}\cdot\text{mol}^{-1}$ . The activation energy should be related to a reaction barrier in the process described in Fig. 2, since a diffusion-limited  $k_2$  would be several times larger than the observed value [29, 31].

Still, our simulation displays a slight overestimation of the rate  $k_2$  compared to experiments. We now discuss the sources of error in our simulation. Firstly, the employed density functional approximation underestimates diffusion. Calculation with our model at 350 K gives diffusion coefficients of  $0.20 \pm 0.02$ ,  $0.30 \pm 0.03$ , and  $0.79 \pm 0.04 \text{ \AA}^2/\text{ps}$  for  $\text{H}_2\text{O}$ ,  $e_{(\text{aq})}^-$ , and  $\text{H}_{(\text{aq})}^+$ , respec-

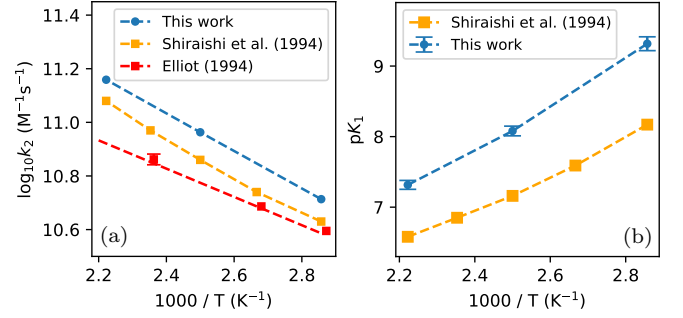


FIG. 3. (a) Arrhenius plot for the predicted  $\log_{10} k_2$  versus inverse temperature, compared with experimental data from Shiraishi et al. [29] and Elliot [30]. (b) van't Hoff plot of the log of the equilibrium constant  $K_1$  versus inverse temperature, compared with the experimental data of Shiraishi et al. [29].

tively. In comparison, the experimental values at room temperature are 0.23, 0.48, and  $0.93 \text{ \AA}^2/\text{ps}$  [31–33], respectively, and these diffusion coefficients are expected to be even higher at 350 K. This, by itself, leads to an underestimation of the diffusion contribution in  $k_2$ , so the overestimation of the overall  $k_2$  should stem from the reaction-controlled contribution, which is also ultimately determined by the underlying density functional. Another remark is that our simulation is run with NVT at  $1 \text{ g}/\text{cm}^3$ , while the experimental density slightly decreases with temperature. However, within our temperature range, this should be a relatively small effect. An additional source of error comes from neglected nuclear quantum effects, which would presumably increase  $k_2$  due to a slightly delocalized proton. Nevertheless, the ratio of the diffusion coefficients between  $\text{H}_2\text{O}$ ,  $e_{(\text{aq})}^-$ , and  $\text{H}_{(\text{aq})}^+$  in our model is in reasonable agreement with experiment, so the qualitative picture, as well as the temperature dependence, should remain physically consistent.

*Equilibrium constant.* In addition to  $k_2$ , Reaction (1) is also characterized by its equilibrium constant, denoted  $K_1$ . This can be calculated from the expression [34, 35]

$$pK_1 = \log_{10} c_0 \int_0^{r_c} e^{-\beta(W(r)-W(r_c))} 4\pi r^2 dr, \quad (8)$$

which relates  $K_1$  to the potential of mean force  $W(r)$ , a function of the distance  $r$  between  $\text{H}^+$  and the electron center  $\mathbf{c}_{e^-}$ . When  $r$  is around zero, it represents the state of  $\text{H}_{(\text{aq})}^+$ . Beyond a certain distance  $r_c$ ,  $W(r)$  plateaus and  $W(r_c) = W(\infty)$ , representing independent  $e_{(\text{aq})}^-$  and  $\text{H}_{(\text{aq})}^+$ .  $c_0 = 1 \text{ M}$  is the standard concentration. The excess  $\text{H}^+$  is identified as the remaining hydrogen after assigning two closest hydrogens to each oxygen atom.

Enhanced sampling is required to determine  $W(r)$ , as the backward reaction is not spontaneous. Here, we use the value of  $V_{\text{emb}}$  at the position of  $\text{H}^+$  as our collective variable (CV). This reflects the electrostatics of the solvent and is well correlated with the progress of the re-

action, where  $V_{\text{emb}}(\text{H}^+)$  is low in the product state  $\text{H}\cdot_{(\text{aq})}$  and increases as  $\text{H}^+$  and  $\text{e}^-$  start to separate. We add a bias potential to raise the free energy corresponding to  $\text{H}\cdot_{(\text{aq})}$  [36], making the reaction reversible within our simulation time. Then, from the biased molecular dynamics simulation,  $W(r)$  and (8) can be evaluated using the properly weighted histogram of the trajectory.

We perform the calculation at 350, 400, and 450 K with up to 512  $\text{H}_2\text{O}$  molecules plus one proton and one electron. We find an acceptable convergence of  $W(r)$  for the 512  $\text{H}_2\text{O}$  size, with  $r_c$  set to 10 Å. A van 't Hoff plot of  $\text{p}K_1$  against inverse temperature is shown in Fig. 3(b). Our  $\text{p}K_1$  decreases from 9.3 at 350 K to 7.3 at 450 K; the positive slope of  $\text{p}K_1$  vs  $T^{-1}$  indicates an endothermic reaction, and the magnitude of the slope agrees well with experiment [29]. We also observe a small positive curvature consistent with experimental trends, which has been proposed to be related to a decrease in the dielectric constant of water at higher temperatures [29]. At 350 K,  $\text{p}K_1 = 9.3$  corresponds to a reaction free energy of 0.65 eV, which is overestimated by 0.07 eV compared to experiment. We also remark that the same reaction in vacuum, the ionization of a hydrogen atom, takes an energy of 13.6 eV. This underscores the dramatic stabilization effect provided by the solvent environment.

**Conclusion.** We have developed an electron-aware machine-learning method to model  $\text{e}^-_{(\text{aq})}$  and its reaction with  $\text{H}^+_{(\text{aq})}$ , relying on a physics-motivated electrostatic embedding to solve for the excess electron. The model is accurate, robust, efficient, and extensible. It exhibits a proton transfer mechanism, and we determine the reaction rate and equilibrium constant over a temperature range, with results in agreement with experiments. Assessment of more accurate electronic structure methods, nuclear quantum effects, and the detailed analysis of the transition state are left for future work. In addition, we expect our method to naturally apply to a broad class of solvated-electron reactions. It would also be interesting to extend the framework to nonadiabatic electron transfer processes, small polarons, bound excitons, and other situations where explicit electron modeling is important.

**Data availability.** The data and the trained model used in this work are available at Zenodo [37]. The code for DPLR-q is available on GitHub [38].

**Acknowledgements.** R.G. and R.C. were supported by the Computational Chemical Science Center: Chemistry in Solution and at Interfaces funded by the U.S. Department of Energy (DOE) under Award No. DE-SC0019394, and by a gift from Seven Research. P.X. was supported by the DOE Advanced Scientific Computing Research (ASCR) Applied Mathematics program under Contract No. DE-AC02-05CH11231. This research used resources of the National Energy Research Scientific Computing Center (NERSC), a U.S. DOE Office of Science User Facility operated under Contract No. DE-SC0019394 and

No. DE-AC02-05CH11231.

- 
- [1] J. Behler and M. Parrinello, Phys. Rev. Lett. **98**, 146401 (2007).
  - [2] K. Schütt, P.-J. Kindermans, H. E. Sauceda Felix, S. Chmiela, A. Tkatchenko, and K.-R. Müller, Adv. Neural Inf. Process. Syst. **30** (2017).
  - [3] L. Zhang, J. Han, H. Wang, R. Car, and W. E, Phys. Rev. Lett. **120**, 143001 (2018).
  - [4] S. Batzner, A. Musaelian, L. Sun, M. Geiger, J. P. Mailoa, M. Kornbluth, N. Molinari, T. E. Smidt, and B. Kozinsky, Nat. Commun. **13**, 2453 (2022).
  - [5] L. Zhang, M. Chen, X. Wu, H. Wang, E. Weinan, and R. Car, Phys. Rev. B **102**, 041121 (2020).
  - [6] L. Zhang, H. Wang, M. C. Muniz, A. Z. Panagiotopoulos, R. Car, and W. E, J. Chem. Phys. **156**, 124107 (2022).
  - [7] J. Lan, V. Kapil, P. Gasparotto, M. Ceriotti, M. Iannuzzi, and V. V. Rybkin, Nat. Commun. **12**, 766 (2021).
  - [8] J. Lan, V. V. Rybkin, and A. Pasquarello, Angewandte Chemie **134**, e202209398 (2022).
  - [9] R. Gao, Y. Li, and R. Car, Phys. Chem. Chem. Phys. **26**, 23080 (2024).
  - [10] See Appendix F for the limitations of these approaches.
  - [11] U. Schindewolf, Angew. Chem., Int. Ed. Engl. **7**, 190 (1968).
  - [12] J. M. Herbert and M. P. Coons, Annu. Rev. Phys. Chem. **68**, 447 (2017).
  - [13] G. Choppin, J.-O. Liljezin, J. Rydberg, and C. Ekberg, *Radiochemistry and nuclear chemistry* (Academic Press, 2013).
  - [14] E. J. Hart and M. Anbar, *The Hydrated Electron* (Wiley-Interscience, New York, 1970) p. 267.
  - [15] R. Car and M. Parrinello, Phys. Rev. Lett. **55**, 2471 (1985).
  - [16] O. Marsalek, T. Frigato, J. VandeVondele, S. E. Bradforth, B. Schmidt, C. Schütte, and P. Jungwirth, J. Phys. Chem. B **114**, 915 (2010).
  - [17] J. Schnitker and P. J. Rossky, J. Chem. Phys. **86**, 3462 (1987).
  - [18] L. Turi and D. Borgis, J. Chem. Phys. **117**, 6186 (2002).
  - [19] L. D. Jacobson and J. M. Herbert, J. Chem. Phys. **133** (2010).
  - [20] N. Marzari, A. A. Mostofi, J. R. Yates, I. Souza, and D. Vanderbilt, Rev. Mod. Phys. **84**, 1419 (2012).
  - [21] F. Ambrosio, G. Miceli, and A. Pasquarello, J. Phys. Chem. B **120**, 7456 (2016).
  - [22] F. Ambrosio, G. Miceli, and A. Pasquarello, J. Phys. Chem. Lett. **8**, 2055 (2017).
  - [23] M. Pizzochero, F. Ambrosio, and A. Pasquarello, Chem. Sci. **10**, 7442 (2019).
  - [24] Y. Zhang, H. Wang, W. Chen, J. Zeng, L. Zhang, H. Wang, and E. Weinan, Comput. Phys. Commun. **253**, 107206 (2020).
  - [25] N. Agmon, Chem. Phys. Lett. **244**, 456 (1995).
  - [26] D. Chandler, in *Classical and Quantum Dynamics in Condensed Phase Simulations* (World Scientific, 1998) pp. 25–49.
  - [27] P. Collet, S. Martínez, and J. San Martín, *Quasi-stationary distributions: Markov chains, diffusions and dynamical systems* (Springer Science & Business Media,

- 2012).
- [28] As in Refs. [21, 22], we simulate only at 350 K and above to enable a “frank diffusive motion” of water, since this DFT functional can show glassy behavior at lower temperatures.
  - [29] H. Shiraishi, G. R. Sunaryo, and K. Ishigure, *J. Phys. Chem.* **98**, 5164 (1994).
  - [30] A. J. Elliot, *Rate constants and g-values for the simulation of the radiolysis of light water over the range 0-300C*, Research Report (Atomic Energy of Canada Limited, 1994).
  - [31] A. J. Elliot, D. R. McCracken, G. V. Buxton, and N. D. Wood, *J. Chem. Soc., Faraday Trans.* **86**, 1539 (1990).
  - [32] M. Holz, S. R. Heil, and A. Sacco, *Phys. Chem. Chem. Phys.* **2**, 4740 (2000).
  - [33] G. V. Buxton, C. L. Greenstock, W. P. Helman, and A. B. Ross, *J. Phys. Chem. Ref. Data* **17**, 513 (1988).
  - [34] J. E. Davies, N. L. Doltsinis, A. J. Kirby, C. D. Roussev, and M. Sprik, *J. Am. Chem. Soc.* **124**, 6594 (2002).
  - [35] M. Calegari Andrade, R. Car, and A. Selloni, *Proc. Natl. Acad. Sci. U.S.A.* **120**, e2302468120 (2023).
  - [36] This suffices for our equilibrium sampling. It avoids differentiating  $\mathbf{c}_{e-}$  through the iterative eigen-solver and avoids the discontinuity as  $\text{H}^+$  hops, which would arise with a common enhanced sampling algorithm with  $r$  as the CV.
  - [37] Supplementary Data, <https://doi.org/10.5281/zenodo.17684097> (2025).
  - [38] Supplementary Code, <https://github.com/SparkyTruck/dplr-q>, accessed: 2025-11-26.
  - [39] S. Goedecker, M. Teter, and J. Hutter, *Phys. Rev. B* **54**, 1703 (1996).
  - [40] J. VandeVondele and J. Hutter, *J. Chem. Phys.* **127** (2007).
  - [41] M. Guidon, J. Hutter, and J. VandeVondele, *J. Chem. Theory Comput.* **6**, 2348 (2010).
  - [42] T. D. Kühne, M. Iannuzzi, M. Del Ben, V. V. Rybkin, P. Seewald, F. Stein, T. Laino, R. Z. Khaliullin, O. Schütt, F. Schiffmann, *et al.*, *J. Chem. Phys.* **152** (2020).
  - [43] We estimate the error from this deviation as follows. The center mismatch corresponds to a dipole of  $\mu_1 \approx 0.1 \text{ e}\cdot\text{\AA}$ . If it interacts with a typical water dipole of  $\mu_2 \approx 0.6 \text{ e}\cdot\text{\AA}$  at a separation of  $r_{12} \approx 6 \text{ \AA}$ , the resulting mean Coulomb force is  $1.2 \text{ meV}\cdot\text{\AA}^{-1}$  per Cartesian component. This is an order of magnitude smaller than our force RMSE, so its impact on accuracy is minimal. Here,  $r_{12} \approx 6 \text{ \AA}$  is a conservative estimate of the region within which the short-range  $E_{\text{sr}}$  fully resolves interactions. Our neural network for  $E_{\text{sr}}$  has a  $6 \text{ \AA}$  cutoff and one message-passing step, so every atom sees neighbors up to  $12 \text{ \AA}$ , and it is expected to accurately resolve the interactions within  $6 \text{ \AA}$ .
  - [44] I.-C. Yeh and G. Hummer, *J. Phys. Chem. B* **108**, 15873 (2004).



## End Matter

*Appendix A. Details on DFT calculations and model training.* We run all DFT calculations using the hybrid functional PBEh( $\alpha$ ) plus the rVV10 van der Waals correction. The fraction of Fock exchange  $\alpha$  is set to 0.4, and the parameter  $b$  in rVV10 is set to 5.3, as proposed in Ref. [21]. We use the Goedecker–Teter–Hutter pseudopotentials [39], a triple- $\zeta$  polarized basis [40], an 800 Ry cutoff for the expansion of density in plane waves, and the auxiliary density matrix method with the cFIT3 basis set [41]. We perform a spin-polarized calculation, as implemented in the CP2K package [42].

To generate an initial DFT dataset, we start with a periodic box of 64 H<sub>2</sub>O molecules at 1 g/cm<sup>3</sup> in an NVT ensemble at 350 K. A proton is added and equilibrated for 200 fs. We then add an excess e<sup>−</sup>, whose initial ground state is delocalized. Within 200–400 fs, e<sup>−</sup> creates a cavity to localize itself, forming e<sup>−</sup><sub>(aq)</sub> [23]. We prepare 15 such initial configurations and run DFT trajectories in parallel for 10–20 ps each; a few of them end up reacting within this timescale. From these trajectories, we extract  $3 \times 10^4$  configurations covering both reactant and product states as our initial training data.

We first train an initial model on this dataset. It enables the active learning process, where we run simulations with our model and sample additional configurations using a model deviation metric [24]. In total, about 1,300 additional configurations are added to the dataset. The final dataset contains 31,518 configurations of 64 water molecules plus one proton and one electron, which we use to train the production model. Validation errors are reported using a 90%–10% train–validation split of the final dataset. Figure 4 compares model-predicted total energies and forces with DFT values and demonstrates the excellent accuracy and generalization of our model.

*Appendix B. Selection of the Gaussian smoothing parameter.* In the Gaussian smoothing of  $\rho_{\text{emb}}$  using the kernel  $e^{-(\beta r)^2}$ , we find that a smaller  $\beta$  (stronger smoothing) increases the deviation of the modeled center  $\mathbf{c}_{e^-}$  from the MLWF center, whereas a larger  $\beta$  requires a denser grid for convergence. We adopt  $\beta = 2 \text{ \AA}^{-1}$  with a grid spacing of about 0.26 Å, which balances these factors. The resulting average distance between  $\mathbf{c}_{e^-}$  and the MLWF center is 0.10 Å [43]. The two terms  $E_{\text{se}}$  and  $E_{\text{lr}}$  partially cancel due to the screening of water around e<sup>−</sup><sub>(aq)</sub> or the proton’s charge in H<sup>+</sup><sub>(aq)</sub>. A different smoothing parameter  $\beta_{\text{lr}} = 0.6 \text{ \AA}^{-1}$  is used in the calculation of  $E_{\text{lr}}$  to numerically minimize  $|\nabla_{\mathbf{R}}(E_{\text{se}} + E_{\text{lr}})|$  and thus enhance this cancellation. Eventually,  $\nabla_{\mathbf{R}}E_{\text{sr}}$  remains the primary contributor to the forces. The precise values of  $\beta$  and  $\beta_{\text{lr}}$  are not critical within a reasonable range, since any differences would be absorbed into  $E_{\text{sr}}$ .

*Appendix C. Investigating the energy and spatial spread of the excess electron.* In Fig. 5, we plot (a) the mod-

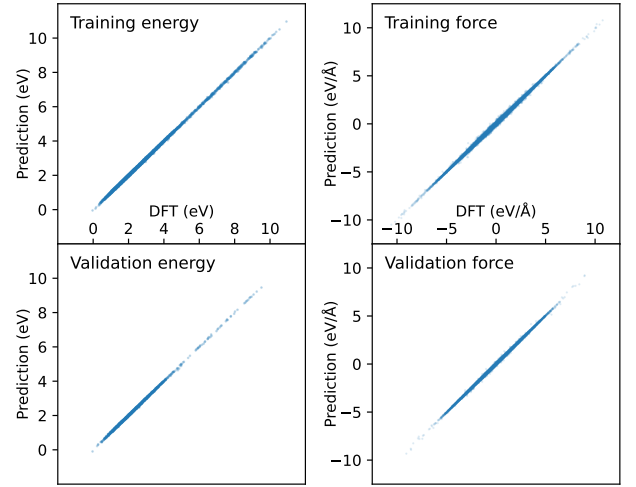


FIG. 4. Parity plots of the total energy and force from DFT vs the trained DPLR-q model for both training and validation data. The energy is shifted to be positive.

eled electron’s energy  $E_{\text{se}}$  versus the Kohn-Sham energy level of e<sup>−</sup> and (b) the modeled electron’s spread versus the MLWF spread of e<sup>−</sup> from DFT. We also indicate the distance  $r$  between H<sup>+</sup> and e<sup>−</sup> by color. For an isolated e<sup>−</sup><sub>(aq)</sub>, the Kohn-Sham energy level lies well within the band gap, typically about 2–3 eV below the conduction band minimum, and the MLWF spread fluctuates around 2 Å. During the reaction, the Kohn-Sham energy level decreases to just slightly above the valence band maximum, and the MLWF spread drops to just under 1 Å. The modeled energy and spread are correlated with the DFT counterparts but are not exactly equal. The range of energy variation is similar, and the spread variation for  $n_{e^-}$  is somewhat smaller than that in DFT. This behavior likely reflects the absence of self-interaction in our one-electron Schrödinger equation (6), whereas DFT, even at the hybrid level, still retains some residual self-interaction. Again, as long as the center  $\mathbf{c}_{e^-}$  agrees with the MLWF center, these differences are short-ranged and are absorbed by the neural network in  $E_{\text{sr}}$ .

*Appendix D. Details of the reaction-rate calculation.* An example of the obtained log-survival probability versus time is shown in Fig. 6(a). One can see a clear linear behavior, where the slope is equal to  $\lambda$ . We remark that if the initial configurations are not sampled from the QSD, the log-survival probability would be curved, and the estimation of  $\lambda$  would be biased. In Fig. 6(b), we show the extrapolation of the rate constant  $k_2$  to the dilute limit. We fit the results from the calculations of 64, 128, 256, and 512-H<sub>2</sub>O molecules. From our numerical results, the finite-size error scales approximately as  $1/L$ , reminiscent of the hydrodynamic finite-size correction to the diffusion constant under periodic boundary conditions [44].

*Appendix E. Details of the equilibrium-constant calculation.* We first plot  $V_{\text{emb}}(\text{H}^+)$  versus the Kohn-Sham

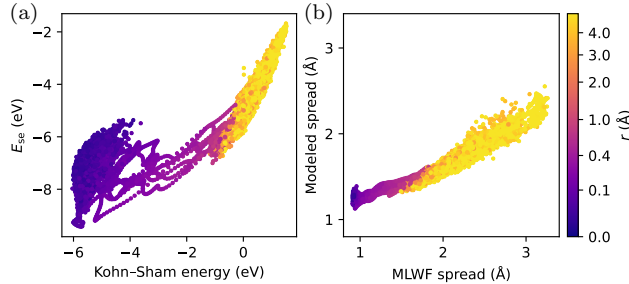


FIG. 5. Modeled electron’s energy and spatial spread compared to the Kohn-Sham energy and MLWF spread from DFT. These plots are based on the initial DFT trajectories in our training data. The distance  $r$  between  $\text{H}^+$  and  $\text{e}^-$  is indicated by color.

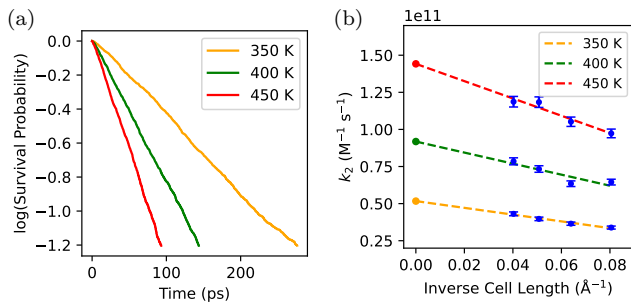


FIG. 6. (a) The obtained  $\ln(\hat{s}(t))$  using a 512- $\text{H}_2\text{O}$  system and 2000 independent trajectories. (b) Extrapolation of  $k_2$  to the dilute limit.

energy of  $\text{e}^-$  in Fig. 7(a) using the data from DFT trajectories. The upper right blob corresponds to cases where the identified proton is not a neighbor of  $\text{e}^-$ . The lower branch is the reaction pathway of interest, with the two quantities tightly correlated. This suggests that  $V_{\text{emb}}(\text{H}^+)$  can serve as a CV for equilibrium sampling. The product  $\text{H}_{(\text{aq})}$  corresponds to  $V_{\text{emb}} \approx -30$  eV. We add a bias that lifts the region below  $\sim -25$  eV to sample both reaction directions. The precise value of  $V_{\text{emb}}(\text{H}^+)$  is not physically relevant, because it is  $\beta$ -dependent.

In Fig. 7(b), we plot the obtained potential of mean force  $W(r)$  for different system sizes at 400 K as an example. Our sampled trajectory is reweighted to the Boltzmann distribution according to the bias potential, and  $W(r)$  is obtained from the logarithm of the sample histogram. The curves are normalized such that  $W(0) = 0$ , and we plot up to half of the box length. We see acceptable convergence at the 512- $\text{H}_2\text{O}$  size. The Coulombic attraction between  $\text{e}_{(\text{aq})}^-$  and  $\text{H}_{(\text{aq})}^+$  is well screened by water, leaving a vanishingly small tail in  $W(r)$  at large  $r$ . The peak around 2 Å is due to the discontinuous

change in the identity of  $\text{H}^+$ ; thus, the histogram contains few samples in this region, and the resulting free energy exhibits a peak. Nevertheless, the evaluation of  $pK_1$  through the integral in (8) remains well-defined and unaffected by such discontinuities.

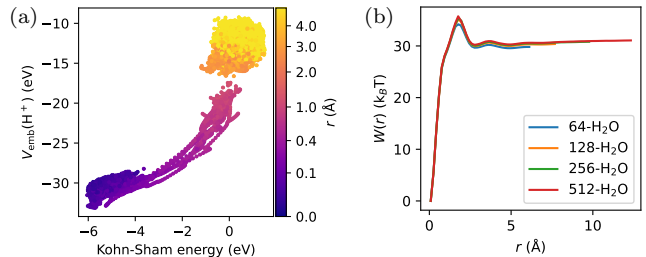


FIG. 7. (a)  $V_{\text{emb}}(\text{H}^+)$  vs DFT energy of  $\text{e}^-$ . The distance  $r$  between  $\text{H}^+$  and  $\text{e}^-$  is indicated by color. (b) Potential of mean force  $W(r)$  at 400 K for different system sizes.

*Appendix F. Comments on the failure of a standard neural network potential.* It is difficult for a neural network potential alone to learn the reaction process, although this is not obvious a priori. Even if the electron is not represented, it may still be implicitly inferred from the modified atomic environment surrounding the cavity. One may thus believe that this would, in principle, allow an ML force field to correctly propagate the dynamics of the system. However, when we train such a force field and run molecular dynamics simulations, we find that it is at risk of occasionally losing track of the local structure around  $\text{e}_{(\text{aq})}^-$ , causing the configuration to collapse to pure water. Once this happens, it is difficult for the system to recover the  $\text{e}_{(\text{aq})}^-$  state, and even if it does, such dynamics cannot be reproduced by DFT and should not have occurred in the first place. Attempts have been made for a system of  $\text{e}_{(\text{aq})}^-$  in water [9], where such failures are mitigated by leveraging a more powerful neural network. However, we find that for modeling reaction (1), where the  $\text{H}^+$  further complicates the system, it remains difficult to eliminate such failures on nanosecond timescales. In our attempts, there is little sign of improvement when we further enhance the neural network or add more training data with active learning. We also note that in Refs. [7, 8], ML models for  $\text{e}_{(\text{aq})}^-$  have been trained; however, the former is limited to a small simulation cell and is not extensible to larger systems, while the latter is not a standalone ML force field and requires DFT calculations to aid the simulation. Overall, we take the view that a more physical treatment of  $\text{e}^-$ , where the electrostatics responsible for its localization is explicitly modeled, offers a more reliable route than relying on purely data-driven neural-network fitting.